Analyst

Accepted Manuscript

This article can be cited before page numbers have been issued, to do this please use: S. Tian, Y. Li, J. Yao, C. Huan, W. Zhang, S. Li, Z. Zhang, Z. Guo, Q. Yang, C. Li, C. Li, J. Li and L. Zhou, *Analyst*, 2025, DOI: 10.1039/D5AN00534E.

View Article Online
DOI: 10.1039/D5AN00534E

ARTICLE

Barcode specific immobilization interface for microfluidics-assisted spatial analysis microarray uniform barcoding

Received 00th January 20xx,
Accepted 00th January 20xx

DOI: 10.1039/x0xx00000x

Sidi Tian,[ab] Yingxue Li,[b] Jia Yao,[b] Changxiang Huan,[ab] Wei Zhang,[b] Shuli Li,[b] Zhiqi Zhang,[b] Zhen Guo,[b] Qi Yang,[b] Chao Li,[b] Chuanyu Li, *[b] Jinze Li*[b] and Lianqun Zhou*[ab]

Microfluidics-assisted spatially barcoded microarray technology offers a high-throughput, low-cost approach to spatial transcriptomic profiling. A uniform barcoded microarray is crucial for spatially unbiased mRNA analysis. However, non-specific adsorption of barcoding reagents in microchannels occurs during liquid transport, causing nonuniform barcoding in chip functional regions. The uneven microarray further leads to biased transcriptome capture. Herein, we develop a barcode specific immobilization (BarSI) interface with both anti-adsorption property and biological activity for the development of uniform spatially barcoded microarray chips. We immobilize DNA probes in straight and serpentine microchannels with coefficient of variation (CV) of 2.3% and 3.2%. Based on the orthogonal barcoding system, we develop spatially barcoded microarray chips with an overall fluorescence intensity CV of 8.47 ± 1.26%, compared with the CV of 20.91 ± 2.84% of microarrays developed on conventional amino glass slides. Using the uniform spatially barcoded microarray chip, we achieve spatially unbiased detection of mouse liver mRNA with the absolute value of Moran's I below 0.05. We present an economical and accessible method for manufacturing uniform spatially barcoded microarray chips, introducing a novel strategy for unbiased transcriptome analysis.

Introduction

Spatially barcoded microarray chip plays a crucial role in spatial transcriptomic profiling by capturing mRNA molecules from tissues and assigning them spatial coordinates using a DNA barcoding system.[1–6] Among spatially barcoded microarray chip technologies, microfluidics-assisted systems demonstrate superior capability in transcriptome analysis of heterogeneous specimens (with diverse sizes, shapes and resolution demands), enabled by custom microchannel architectures and flexible geometries.[7,8] Decoder-seq adopts a microfluidics-assisted barcoding strategy, applying microchannels with varying widths (10, 15, 25, 50 μm) to deliver barcode reagents and generate DNA microarrays on functionalized glass slides.[9] The Xi-Yi combinatorial method simplifies the fabrication of spatially barcoded microarrays and avoids decoding steps. Benefiting from the flexible geometries of microchannels, the barcoding area of chips can be significantly expanded. By extending microchannel length and interconnecting barcoding regions through serpentine intersecting channels, researchers improve barcoding efficiency by two orders of magnitude and broadened the capture area via the fusion of multiplegrid.[10] Microfluidics-assisted spatially barcoded technologies offer a high-throughput, convenient strategy for the fabrication of custom barcoded microarray chip.

However, the transport of barcode reagents containing biomolecules in microchannels is strongly affected by hydrophobic interactions, causing biomolecules to be adsorbed in microchannels, thereby altering local concentrations and affecting chip functionality[11–13]. As microchannel length increases and complex geometries are introduced, the microchannel surface to-volume ratio continues to increase, raising the probability of molecular interactions with the microchannels.[14] This adverse effect caused by adsorption is further amplified, resulting in nonuniform DNA barcodes immobilization of the chip barcoding regions and spatially biased mRNA capture. The non-specific adsorption of biomolecules represents a significant challenge for the application of microfluidic devices,[15,16] leading to the development of various surface coating technologies to reduce non-specific adsorption[17–19]. In microfluidics-assisted microarray chip technology, glass slide is often used as the substrate for the microchannel and serves for DNA probes immobilization because of its optical transparency, rigidity, and biocompatibility.[20,21] Whereas the exposed hydroxyl groups on the glass slide lead to non-specific adsorption of biomolecules,[22,23] they create reactive sites for grafting various anti-adsorption molecules[24]. As a gold-standard protein-resistant surface coating, poly(ethylene glycol) (PEG) is often grafted onto substrate surfaces to reduce non-specific adsorption.[25] Researchers have grafted PEG-silane to the silanol groups on the glass slide to create a low-adsorption interface[26], owing to the barrier formed by water molecules tightly bound around the long PEG chains[27]. Similarly, polymer chains grafted onto the glass slide through reactive silanol groups stabilize lubricating molecules via dynamic dipole-dipole interactions, forming a slippery polymeric surface that effectively suppresses protein adhesion.[28]

[a] School of Biomedical Engineering (Suzhou), Division of Life Sciences and Medicine, University of Science and Technology of China, 230026 Hefei, China
[b] CAS Key Lab of Bio-Medical Diagnostics, Suzhou Institute of Biomedical Engineering and Technology, Chinese Academy of Sciences, 215163 Suzhou, China
Supplementary Information available: [details of any supplementary information available should be included here]. See DOI: 10.1039/x0xx00000x

View Article Online
DOI: 10.1039/D5AN00534E

For the development of microfluidic-assisted microarray chips, the immobilization of DNA probes on substrates forms the foundation of chip barcoding.[29] Covalent bonding between functionalized interfaces and DNA strands with modified ends enables stable microarray development with controlled molecular orientation.[30] The covalent immobilization of amine-modified DNA for microarray fabrication can be achieved through functionalization of glass slide with amino, carboxyl, aldehyde, or EDC/NHS ester groups.[31–34] The development of three-dimensional (3D) nanosubstrates with high aspect ratios on functionalized interfaces provides additional active sites for DNA probe immobilization, thereby further enhancing microarray density.[9,35] However, active groups (amino, NHS ester or silanol groups) on the interface can induce non-specific adsorption of biomolecules through intermolecular interactions such as electrostatic forces or hydrogen bonding, which may compromise microfluidics-assisted microarray barcoding.[36–38]

Maintaining both anti-adsorption capability and chemical reactivity on the same interface is contradictory.[39] Hydrophobic/superhydrophobic interfaces are widely applied for anti-adsorption, yet the low surface energy restricts effective biomolecule immobilization. Li et al. achieved microarray immobilization on hydrophobic surfaces by modifying silicon nanofibers via photo click thiol-ene reactions.[40] Meneses et al. developed nucleic acid microarrays using fluor-thiol photocoupling reactions on low surface energy substrates.[41] However, in hydrophobic microchannels, the capillary pressure generated by surface tension affects the transportation stability of liquid, and this negative effect becomes more intense as the channel size decreases.[42] Furthermore, the use of complex instruments makes these approaches difficult to apply in highly parallelized chip barcoding processes. Therefore, a bioactive interface that simultaneously suppresses non-specific adsorption and enables covalent DNA barcode immobilization is required, designed for the fabrication of a microfluidic-assisted uniform spatially barcoded microarray.

In this study, we develop the barcode specific immobilization (BarSI) interface based on combined silane modification for the fabrication of microfluidics-assisted uniform spatially barcoded microarray chips (Fig. 1). Given the chemical versatility and commercial availability of silane coupling agents[43], we treat glass slides with a combination of 3-glycidyloxypropyltrimethoxysilane (GPTMS) and 2-cyanoethyltriethoxysilane (CETES). GPTMS enables covalent immobilization of DNA barcodes through epoxide-amine ring-opening reactions, while CETES replaces surface exposed silanol groups on glass slide to suppress non-specific adsorption. As a structural component of the microchannels, poly-dimethylsiloxane (PDMS) is further treated with mPEG-silane to reduce non-specific adsorption during reagent transport. We form a uniform spatially barcoded microarray chip with a coefficient of variation (CV) of 8.47 ± 1.26%. Furthermore, we used mouse liver mRNA to validate the unbiased detection capability of the chip. Our work presents a novel approach for the fabrication of uniform spatially barcoded microarray chips, offering a new strategy for unbiased transcriptome analysis.

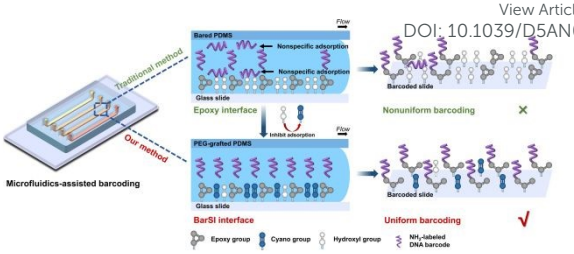

Fig. 1 Working principle of the barcode specific immobilization interface.

2 Experimental section

2.1 Materials

The brands and catalog numbers of all materials and reagents were listed in Table S1.

All oligonucleotide probes were synthesized by GENEWIZ (China), and the sequences were provided in Table S2 and Table S3.

2.2 Design and fabrication of microfluidic devices

We designed and fabricated a PDMS chip demolding device. This device consisted of an aluminum clamp and a silicon wafer. The microchannel layout was designed using AutoCAD and etched onto the silicon wafer through UV lithography. Both the aluminum clamp and the silicon wafer were treated with a hydrophobic coating to facilitate PDMS demolding. The PDMS chips were fabricated by repeatedly casting PDMS on the demolding device. The PDMS base and curing agent were thoroughly mixed at a 10:1 ratio. A vacuum pump was used to remove bubbles from the mixture, which was then poured into the demolding device. After further degassing with the vacuum pump, transferred the demolding device to an oven and cure at 80°C for 1 h. Carefully peeled off the cured PDMS chip and punched through each inlet and outlet.

After punching, the PDMS chip was reversibly bonded to a silane-functionalized glass slide and placed it into the sample loading device for liquid injection. The sample loading device consisted of an aluminum clamp and a vacuum pump. The vacuum pump was connected to the aluminum clamp via a Teflon tube to enable liquid injection under negative pressure. The aluminum clamp secured the microfluidic chip to prevent liquid leakage.

2.3 Silanization of glass slides and PDMS microchannels

The clean and dry glass slides (76 mm × 26 mm) that had been ultrasonically cleaned were placed into a piranha solution for 10 min to expose abundant silanol groups. After rinsing with DI water, the glass slides were dried with nitrogen gas. The glass slides were immersed in ethanol solutions (anhydrous ethanol/DI water = 95:5, v/v) containing different concentrations of silane coupling agents and incubated on a shaker at room temperature for 5 h. For conventional amino glass slides, a 5% 3-aminopropyltriethoxysilane solution in anhydrous ethanol was used.[9] Subsequently, the glass slides

View Article Online
DOI: 10.1039/D5AN00574E

were rinsed three times (5 min each) with anhydrous ethanol and dried with nitrogen gas. Finally, placed the glass slides in a vacuum oven at 110°C for 1 h. The silane-functionalized glass slides were stored in a desiccator until use.

The demolded PDMS was ultrasonically cleaned in anhydrous ethanol for 10 min and dried with nitrogen gas. The clean and dry PDMS was treated with a plasma cleaner to expose abundant silanol groups. The PDMS was reversibly bonded to a clean and dry glass slide (not treated with piranha solution or silanization), introduced mPEG-silane solution (2% w/v) into the microchannels[44], and incubated on a shaker at room temperature for 5 h. The PDMS was rinsed three times (5 min each) with anhydrous ethanol and dried with nitrogen gas. Finally, placed the PDMS in a vacuum oven at 110°C for 1 h and allowed it to cool overnight under vacuum. Stored the mPEG-silane-functionalized PDMS in a desiccator until use.

2.4 Characterization of the anti-adsorption property of PEG-grafted PDMS microchannels

The PDMS chip with or without mPEG-grafting was reversibly bonded to a clean and dry glass slide (not treated with piranha solution or silanization). A 1 mg/mL FITC-labeled BSA solution or a 2 μM Cy3-labeled DNA probe solution was introduced into the microchannels and incubated for 1 h to simulate the reaction time. The microchannels were then rinsed with DI water and dried with nitrogen gas. Residual fluorescence signals in the microchannels were detected using a NIKON super-resolution confocal laser-scanning microscope system AX with NSPARC at 488 nm (for BSA) and 560 nm (for the DNA probe).

2.5 Filling time measurement

The PDMS was reversibly bonded to silane-functionalized glass slides under different treatments and fixed using an aluminum clamp. The vacuum pump pressure was set to -30 kPa and connected to the aluminum clamp via Teflon tubes. A high-speed camera was connected to a microscope with a 4× objective to directly observe the liquid transport and record the time taken for the fluid meniscus front to reach the end of the microchannel. The average flow velocity in microchannels with different modifications was calculated as the total microchannel length divided by the filling time.

2.6 Optimization of probe immobilization uniformity

After obtaining silane-functionalized glass slides and PDMS chips treated under different conditions, the uniformity of probe immobilization was verified in both straight and serpentine microchannels. A 2 μM Cy3-labeled probe solution was introduced into the microchannels, with the injection time defined as the time required for the liquid to completely fill the microchannel. After incubation for 12 h, the PDMS chip was removed. The glass slides were washed three times at 55°C with a washing buffer (2× SSC, 0.1% SDS), rinsed with DI water, and finally dried with nitrogen gas. Fluorescence images of probe immobilization in the microchannels were captured using the Olympus SLIDEVIEW VS200. The fluorescence intensity at different positions were analyzed using ImageJ software. For the batch-to-batch reproducibility tests and storage stability tests, the ratio of the fluorescence intensity difference between the inlet and outlet of the microchannel to the inlet fluorescence intensity was defined as fluorescence variation.

2.7 Barcoding of microfluidic chips

The barcoding of the microfluidic chip was achieved through a orthogonal barcoding system. First, the PDMS chip X (with straight microchannels) was aligned and placed on a silane-functionalized glass slide, and barcode X solutions (X1-X35, 2 μM) were introduced into each microchannel under -30 kPa pressure. The chip was incubated overnight to complete the immobilization of barcode X. The PDMS chip X was then removed, and the glass slide was washed three times at 55°C with a washing buffer, rinsed with DI water, and finally dried with nitrogen gas. Next, the PDMS chip Y (with serpentine microchannels) was aligned and placed on the glass slide, and 2 μL of barcode Y solutions (Y1-Y35, containing 2 μM barcode Y, 2 μM Cy3-labeled linker and 1.5× ligase) were introduced into each microchannel. The reaction proceeded for 1 h to complete the ligation of barcode Y. The PDMS chip Y was then removed, and the glass slide was washed three times at 55°C with a washing buffer, rinsed with DI water, and finally dried with nitrogen gas.

After barcoding, fluorescence images of the microarray were captured using the Olympus SLIDEVIEW VS200. The grayscale values of the microarray were analyzed using a digital image processing algorithm based on morphological analysis, implemented through Python programming.

2.8 Microarray UMI statistics

The chip barcoding area was assembled with clamps to form a well on the slide without liquid leakage. 70 μL of barcode-elongation solution was added to the well, containing 7 μL of 10× Klenow fragment reaction buffer, 7 μL of Klenow fragment (5 U/μL), 7 μL of dNTP mix (10 mM dATP, 10 mM dTTP, 10 mM dCTP and 10 mM dGTP), and 7 μL of 10 μM Primer-UMIR. The solution was incubated at 37°C for 1 h, after which the reaction

View Article Online
DOI: 10.1039/D5AN00534E

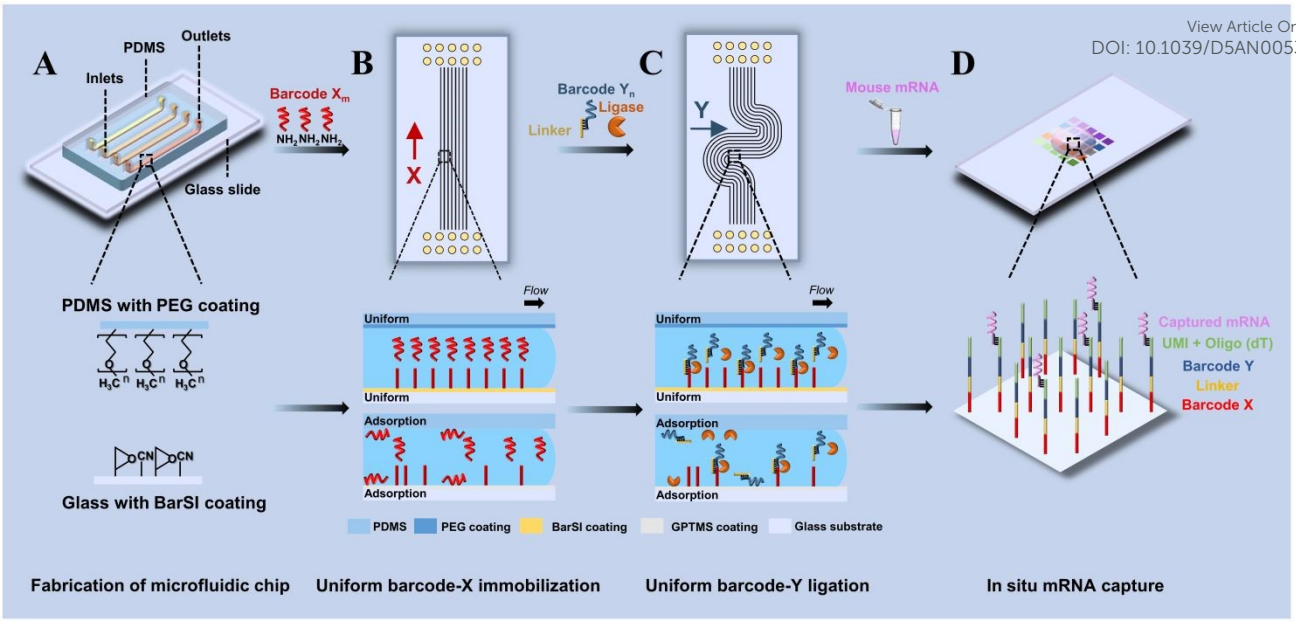

Fig. 2 Workflow for the preparation and optimization of a uniform spatially barcoded microarray chip. (A) The BarSI glass slide and PEG-grafted PDMS were reversibly bonded together to form the microfluidic chip. (B) Barcode X reagent (5'-amino modified barcode X solution) was introduced into the chip and uniformly immobilized onto the surface of the glass slide. (C) The barcode Y reagent (linker, T4 DNA ligase, and barcode Y mixture) was uniformly introduced into the chip and connected with barcode X. (D) A uniform spatially barcoded microarray was formed using a orthogonal barcoding system and applied for mRNA capture.

solution was removed, and the glass slide was washed 3 times with EB buffer. Then, second-strand cDNA was eluted from the barcoding system and applied for mRNA capture array via treatment of 35 µL of 80 mM KOH for 10 min, followed by neutralization with 5 µL of 1 M Tris (pH 7.0).

The collected second-strand cDNA was amplified using the following PCR system: 1× KAPA HiFi HotStart ReadyMix, 1 µM Primer-UMIF, 1µM Primer-UMIR, and second-strand cDNA. The following PCR program was used: 98°C for 3 min, cycled at 98°C for 20 s, 65°C for 30 s and 72°C for 1 min, and a final incubation at 72°C for 5 min. The PCR products were purified using Hieff NGS ® Smarter DNA Clean Beads, and the final concentration was quantified using the Qubit dsDNA Assay Kit. The constructed libraries were sequenced on a NovaSeq 6000 system in PE150 mode. By classifying different barcodes based on barcode X and barcode Y, we counted the types of the 12 bp sequence adjacent to the barcode Y, which represented the number of UMI per spot.

2.9 Tissue collection and cryosection

After tissue collection, the mouse liver was washed with pre-cooled PBS, and the residual moisture was removed. The tissue was then embedded in optimal cutting temperature (OCT) compounds and cooled in liquid nitrogen. The frozen samples were stored at -80°C until sectioning.

The cryostat temperature was adjusted to -20°C, and the samples to be sectioned were placed in the cryostat for at least 30 min to equilibrate. During sectioning, the tissues were first trimmed by 30 µm to the desired position. The 30 µm sections were collected in enzyme-free 1.5 mL centrifuge tubes for RNA integrity (RIN) testing. Then, ten 10 µm sections were prepared and collected in 1.5 mL RNase-free centrifuge tubes for RNA extraction.

2.10 RNA extraction and reverse transcription

Total RNA was extracted from the liver tissues using RNA isolater Total RNA Extraction Reagent, and 1.0 µg of total RNA was diluted with 50 µL Nuclease-free water. The chip barcoding area was assembled with clamps to form a well on the glass slide. Then, 50 µL total RNA was added into the well and incubated at 37°C for 30 min. The reverse-transcription reagent was prepared, containing 14 µL of 5× SSIV Buffer, 3.5 µL of SuperScriptTM^{IV} (200 U/µL), 3.5 µL of dNTP mix (10 mM dATP, 10 mM dTTP, 10 mM dCTP and 10 mM dGTP), 3.5 µL of 100 mM DTT, 3.5 µL of RNaseOUT (40U/µL), 3.5 µL of TSO-RT (50 µM) and 3.5 µL of Nuclease-free water. The reverse-transcription reagent was added to the well and incubated at 50°C for 12 h.

2.11 Secondary strand synthesis

The glass slide was washed with 80 mM KOH for 5 min to remove residual mRNA. The second-strand synthesis reagent was prepared, containing 7 µL of 10× Klenow fragment reaction buffer, 7 µL of Klenow fragment (5 U/µL), 7 µL of dNTP mix (10 mM dATP, 10 mM dTTP, 10 mM dCTP and 10 mM dGTP), 7 µL of 100 µM TSO-RP, and 42 µL of Nuclease-free water.

The second-strand synthesis reagent was added to the well and incubated at 37°C for 2 h. After removing the reagent, the glass slide was washed three times with EB buffer. Then, 35 µL of 80 mM KOH was added to the well to obtain second-strand cDNA. Then, second-strand cDNA was eluted from the microarray via treatment of 35 µL of 80 mM KOH for 10 min, followed by neutralization with 5 µL of 1 M Tris (pH 7.0).

View Article Online
DOI: 10.1039/D5AN00534E

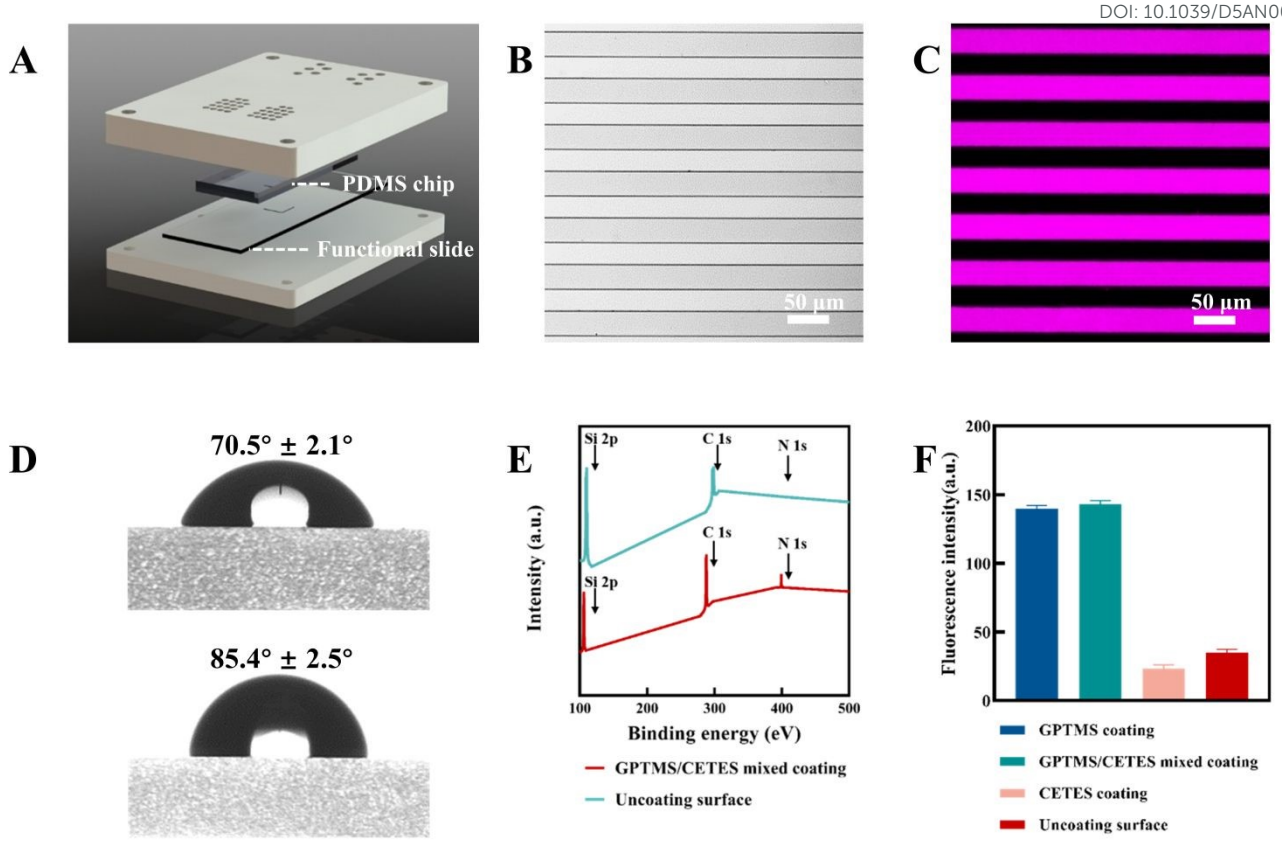

Fig. 3 Preparation and characterization of microfluidic chip. (A) Microfluidic device diagram. The PDMS and glass slide were secured between the top and bottom aluminum clamps to prevent leakage during the sample loading process. The top aluminum clamp contained loading holes (for introducing barcoding reagents) and vacuum holes (connected to a negative pressure device via Teflon tube to facilitate sample loading), which aligned with the corresponding holes on the PDMS. (B) 30 μm width microchannels with rectangular cross-section; scale bar, 50 μm. (C) Immobilization of Cy5-labeled probe in confined space; scale bar, 50 μm. (D) Static water contact angles on bare glass slides (top) and glass slides with the co-treatment of GPTMS and CETES (bottom). n = 3. (E) XPS spectra of glass slides with and without the co-treatment of GPTMS and CETES. (F) Fluorescence intensity evaluation after Cy3-labled probe immobilization on different coatings.

2.12 Amplification, library construction and sequencing

The amplified second-strand cDNA was collected, and the reaction mixture contained 1× KAPA HiFi HotStart ReadyMix, 1 μM Primer-UMIF, 1 μM TSO-RP, and second-strand cDNA. The following PCR program was used: 98°C for 3 min, followed by 20 cycles of 98°C for 20 s, 65°C for 30 s, and 72°C for 1 min, with a final incubation at 72°C for 5 min. The PCR products were purified using Hieff NGS® DNA Selection Beads, and the final con centration was quantified using the Qubit dsDNA Assay Kit. The constructed library was sequenced on the NovaSeq 6000 platform (Illumina) in PE150 mode.

2.13 Moran's I analysis and LISA clustering

The expression matrices of six marker genes were transformed into a 35×35 two-dimensional spatial monitoring matrix, where each cell value represented the TPM expression level at its corresponding spatial coordinate. Subsequently, the matrix was flattened, and a spatial weight matrix was generated based on the Rook adjacency rule. The significance of global spatial autocorrelation was evaluated by calculating the global Moran's I through permutation tests. Finally, local indicator of spatial association (LISA) clustering was performed using the original coordinate based positional data.

3 Results and discussion

3.1 Preparation and characterization of microfluidic chip

The workflow of the microfluidic chip was shown in Fig. 2. The microfluidic chip composed of a glass slide and PDMS was developed, where the glass slide served as the substrate for DNA barcodes immobilization, and PDMS formed the microchannel structure (Fig. 3A). Based on the flexible geometries of microchannels, we developed straight microchannels and serpentine microchannels with a depth of 10 μm and a width of 30 μm, with an interval of 25 μm between

View Article Online DOI: 10.1039/D5AN00534E

adjacent microchannels (Fig. 3B, S2 and S3†). Each PDMS chip contained 36 microchannels, with dye introduced into the outermost microchannels to indicate sample loading. Two perpendicular sets of microchannels were sequentially placed on a silane-functionalized glass slide. Barcodes X were first introduced into the straight microchannels to covalently bind to the silane-functionalized glass slide, followed by the introduction of barcodes Y into the serpentine microchannels to connect with barcodes X. A orthogonal barcoding system was employed to form a barcoded microarray with 1,225 spots, significantly reducing the variety of barcoding reagents and shortening the processing time.

To successfully prepare a uniform spatially barcoded microarray chip, we developed the BarSI interface with both anti-adsorption and probe immobilization capabilities on glass slide. Epoxy-silane and cyano-silane were simultaneously grafted onto the clean glass slide pretreated with piranha solution (to generate hydroxyl groups) in a one-step procedure. The epoxy groups enabled DNA barcodes immobilization through a ring-opening reaction between the epoxy group and the amino group, allowing the covalent attachment of 5'-NH2-labeled barcodes onto the glass slide. Therefore, the barcodes immobilization performance of commonly used epoxy silane coupling agents, 3-glycidyloxypropyltrimethoxysilane (GPTMS) and 3-glycidyloxypropyltriethoxysilane (GPTES), was compared (Fig. S4†). We treated the slides with different concentrations of GPTMS or GPTES from 0 to 15% (v/v), and then used 5'-NH2 and 3'-Cy3 labeled oligonucleotide probes to simulate barcodes immobilization. The fluorescence intensity peak of GPTMS-treated glass slides was higher than that of GPTES-treated glass slides due to the stronger hydrolytic activity of the methoxy groups in GPTMS, resulting in a higher grafting density on the glass slide. To optimize the probe immobilization efficiency, we further investigated the influence of GPTMS-treated glass slides at varying concentrations within the microchannel on the uniformity of probe immobilization (Fig S5†). The result revealed that across all GPTMS concentrations, fluorescence intensity decreased with increasing transport distance due to the absence of co-treatment with cyano-silane. As the GPTMS concentration increased, the initial fluorescence intensity of immobilized probes peaked at 7.5%, indicating saturation of GPTMS grafting. Therefore, 7.5% GPTMS was chosen for epoxy-silanization of the glass slide, and this concentration was used as a baseline for the introduction of cyano-silane. The cyano group, as a Lewis base, rendered the solution slightly alkaline and accelerated the hydrolysis of cyano-silane[45], which replaced the active silanol groups on the glass slide and reduced non-specific adsorption of biomolecules. Meanwhile, the cyano group created a polar aprotic environment on the glass slide, preventing the protonation of the terminal amino groups of biomolecules, thereby facilitating the nucleophilic reaction between amino groups and epoxy groups. 2-cyanoethyltriethoxysilane (CETES) was selected as the inert component, and initially, we treated the glass slides with a combination of CETES and GPTMS at a 1:1 (v/v) ratio. The X-ray photoelectron spectroscopy (XPS) spectra of the glass slides before and after silane co-treated were shown in Fig. 3E. The characteristic peaks including C 1s, Si 2p, and N 1s were detected. Compared with bare glass slides, a distinct N 1s peak was observed due to the successful grafting of CETES on the co-treated glass slides. However, since the difference in carbon content between the slides with or without grafting was minimal, it was difficult to determine whether GPTMS was simultaneously grafted based on XPS results alone. Therefore, the fluorescence intensity of probes immobilization under different treatments was compared (Fig. 3F). We observed that the fluorescence intensity on the co-treated glass slides was similar to that on the GPTMS-treated slides, while the fluorescence intensity on the CETES-treated glass slides was similar to that on the bare glass slides, indicating that GPTMS and CETES were simultaneously grafted onto the glass slides. Since the XPS measurement of the surface coating could be influenced by the substrates, we further measured the contact angles of the glass slides with or without coating to verify the formation of the coating. The contact angles of differently treated glass slides were tested (Fig. 3D). As expected, the contact angle of the co-treated glass slides (85.4° ± 2.5°) increased compared to that of the bare glass slides (70.5° ± 2.1°), due to the replacement of exposed hydroxyl groups on the co-treated slides, leading to reduced hydrophilicity. The above evidence confirmed the simultaneous grafting of GPTMS and CETES onto the glass slides, forming a BarSI interface.

Furthermore, Cy5-labeled probes were introduced into the microchannels to verify the probe immobilization capability within the confined space. The results demonstrated that the probes were immobilized in the shape of the microchannels on the glass slide, with clear boundaries between channels, without diffusion or leakage (Fig. 3C). Based on this, further discussions will be conducted on how changes in interface properties enhance the uniformity of oligonucleotide probes immobilization within the microchannels.

3.2 Uniform probe immobilization in microchannels

Based on previously developed microfluidic chips, we optimized probe immobilization uniformity in both straight and serpentine microchannels with lengths of 40 mm and 60 mm respectively. Differential pressure flow was used to transport barcoding reagents. In rectangular cross-section microchannels, the flow rate and velocity were proportional to the differential pressure between the two ends of the microchannels. For this purpose, -30 kPa pressure was applied at the microchannels outlet to drive liquid transport, which both reduced the time required for sample introduction and avoided channel deformation or leakage caused by excessive differential pressure.

As a structural component of microchannels, PDMS exhibited non-specific adsorption due to its hydrophobic nature, which easily interacted with hydrophobic domains of biomolecules.[46] Therefore, mPEG-silane was grafted onto the PDMS microchannel surface to reduce non-specific adsorption. We separately verified the anti-adsorption effect of PEG-grafted PDMS on oligonucleotide (Cy3-labeled probes) and proteins (FITC-labeled BSA) (Fig. 4A and 4B). Briefly, DNA probe and

View Article Online
DOI: 10.1039/D5AN00534E

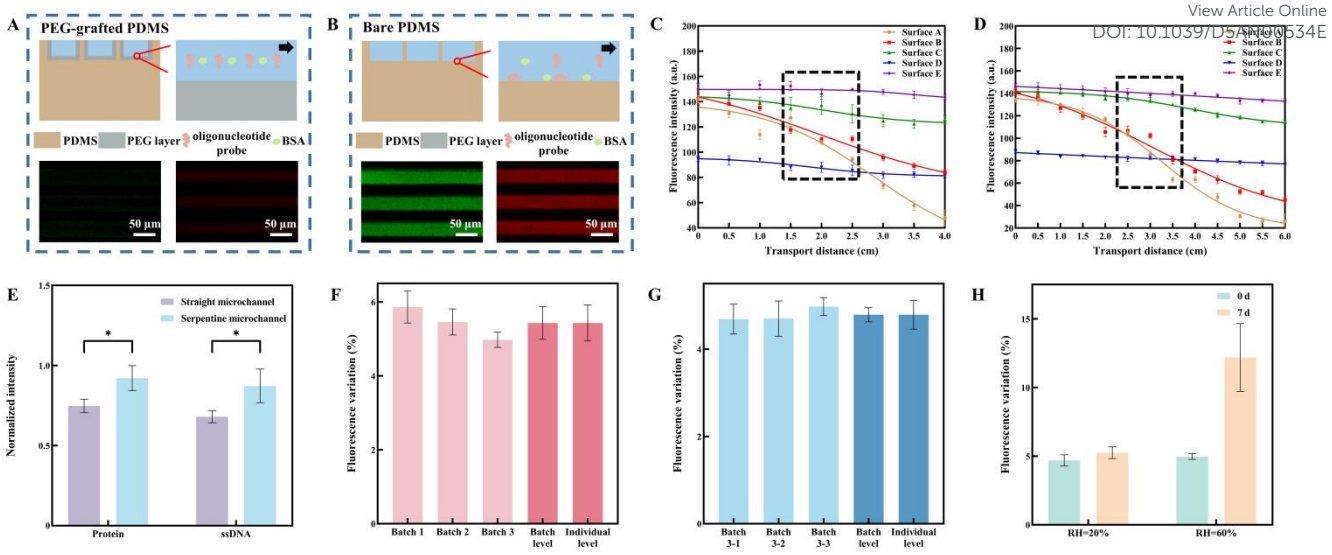

Fig. 4 Optimization of probe immobilization uniformity in microchannels. (A) Reduction of oligonucleotide probe and BSA non-specific adsorption in PEG-grafted PDMS microchannels; scale bar, 50 μm. (B) Oligonucleotide probe (red) and BSA (green) non-specific adsorption in bare PDMS microchannels; scale bar, 50 μm. (C) Variation of probe fluorescence intensity with increasing transport distance in straight microchannels. The dashed box in the figure represented the barcoding region. (D) Variation of probe fluorescence intensity with increasing transport distance in serpentine microchannels. The dashed box in the figure represented the barcoding region. (E) Influence of geometries on the adsorption of proteins and ssDNA. (F) Inter-batch effect tests. (G) Intra-batch effect tests. (H) Storage stability tests. RH represented for relative humidity.

protein reagents were added to the inlets with a continuous flow under - 30 kPa pressure for 10 min to simulate the sample loading process. After incubation at room temperature for 30 min, the microchannels were rinsed with deionized (DI) water. Subsequently, we obtained fluorescence images using a confocal microscope. The results indicated that the bare PDMS surface displayed significant fluorescence signals, whereas the PEG-grafted surface essentially showed no residual DNA probes and proteins, which indicated that the non-specific adsorption caused by PDMS was essentially eliminated.

Further, based on the optimal concentration of GPTMS treatment for glass slides (7.5%), we prepared four surface coatings by introducing CETES and adjusting the ratio of GPTMS to CETES during the glass slides silanization process: First, a surface completely treated by GPTMS (Surface A); second, a surface co-treated by GPTMS-CETES (2:1) (Surface B); third, a surface co-treated by GPTMS-CETES (1:1) (Surface C); and fourth, a surface co-treated by GPTMS-CETES (1:2) (Surface D). We first used untreated PDMS microchannels to introduce the reagents, and used 5'-NH2 and 3'-Cy3 labeled oligonucleotide probes to simulate barcodes immobilization on these four surfaces. After obtaining the surface coating with the most uniform probe immobilization, we introduced PDMS microchannels grafted with mPEG-silane, creating Surface E. We introduced and immobilized probes in both straight and serpentine microchannels, setting the sample introduction time as the filling time. Due to differences in microchannel interface properties under different treatments, the time required to completely fill microchannels with barcoding reagents varied under the same negative pressure conditions. Therefore, we measured the filling time of barcoding reagents in microchannels under different treatments to analyze the time needed to completely fill differentially treated microchannels. The average flow velocities and complete filling times of barcoding reagents in microchannels with different treatments were shown in Fig. S6 and Table S4.†After sample loading, the chip was incubated for 12 h and then washed, and the probes immobilization fluorescence intensity at different positions along the microchannel transport was recorded, as shown in Fig. 4C and 4D. We used the CV to evaluate probe immobilization uniformity in microchannels, with results presented in Table S5†. In both microchannel shapes, the overall fluorescence intensity of Surface D was only half that of the other three surfaces, which might be due to the decreased GPTMS grafting density caused by CETES introduction, reducing probes immobilization density. Among different microchannel shapes, Surface C consistently showed the lowest CV, and therefore we subsequently used PEG-grafted PDMS microchannels to introduce and immobilize probes on Surface C. The results indicated that the fluorescence intensity CV for Surface E were 2.3% and 3.2% in straight and serpentine microchannels, respectively, which were below the industry standard of CV less than 10%.[47]

To validate the effects of microchannel geometries on biomolecule adsorption, we used bare PDMS to analyze the non-specific adsorption in both serpentine and straight microchannels, with the results presented in Fig. 4E. Compared to straight microchannels, serpentine microchannels showed

View Article Online
DOI: 10.1039/D5AN00534E

increases of proteins (23.1%) and DNA probes (28.2%) due to the non-specific adsorption. The increased non-specific adsorption observed in serpentine microchannels can be explained from two aspects. First, compared to straight microchannels, serpentine microchannels had a larger specific surface area, which created more potential adsorption sites; second, the more complex geometric shape of serpentine microchannels enhanced liquid-solid mass transfer, further increasing the solid-phase interface adsorption of biomolecules.[48]

To validate the batch-to-batch reproducibility of the BarSI chips, we analyzed the CV for both inter-batch and intra-batch effects at two levels: batch level (assessing CV between batches) and individual level (assessing CV across all individuals). For inter-batch, the batch-level CV was 8.1% and the individual-level CV was 8.9% (Fig. 4F). For intra-batch, the batch-level CV was 3.4% while the individual-level CV was 6.8% (Fig. 4G). We also conducted the storage stability tests. The results showed that the fluorescence variation increased by 12% after 7 days under dry conditions, with an intra-group CV of 8%. However, under humid conditions, the fluorescence variation increased by 132% after 7 days, with an intra-group CV of 20% (Fig. 4H). These results indicated that the chips remained effective for subsequent experiments after 7 days of storage in dry conditions. The higher CV of chips under humid conditions was likely attributed to hydrolysis of the silane layer in humid environments, leading to probe detachment.

In summary, our experiments demonstrated that on BarSI interface treated with GPTMS-CETES (1:1), DNA probes could be immobilized on interfaces with lengths of 40 mm and 60 mm using PEG-grafted PDMS microchannels of different shapes, with an overall CV less than 10%.

3.3 Barcoding and characterization of spatial microarray chip

After developing the BarSI interface capable of uniform probe immobilization, we first introduced X barcoding reagents (containing barcodes X) into straight PDMS microchannels grafted with mPEG-silane. After immobilizing for 12 h, we removed the straight PDMS microchannels and washed the glass slides. Then, we introduced Y barcoding reagents (containing barcodes Y, Cy3-labeled linker and ligase) into PEG-grafted serpentine PDMS microchannels to form spots, with a reaction time of 30 min. Based on our measurements of microchannel filling times, the barcoding reagents transport times were set to 30 s and 50 s for straight and serpentine microchannels, respectively. Through ligase and Cy3-labeled linker, barcodes Y connected with barcodes X to form a spatially barcoded microarray (Fig. 5A, S7A, S7B and S7C†). The average width of spots in the microarray was 29.99 μm, with an average area of 902.44 μm^2 (Fig. 5B). Each spot in the microarray displayed fluorescence due to the presence of Cy3-labeled linker, so we represented the uniformity of the microarray by detecting the grayscale values of each spot and plotting as a heatmap (Fig. 5C). The results showed that the CV of microarrays' grayscale was 8.47 ± 1.26%, compared with the CV of 20.91 ± 2.84% of microarrays developed on conventional amino glass slides, and 13.3% of 25-μm-microarray in reported paper[9] (Fig. S7D, S7E and S7F†). Simultaneously, we detected the number of barcodes in each spot of the microarray to prove the successful barcoding of the chip. Using oligo(dA) as the primer, the copies of each barcode were generated in situ on the barcoding chip. The theoretical length of spatial barcodes should be 100 bp (Fig. S1†). So the elongation products were amplified, and their fragment sizes were analyzed using capillary electrophoresis (Fig. S8A†). The results showed that the in situ barcode copies matched the theoretical length, and thus the amplicons were subjected to Next-Generation Sequencing (NGS). The results revealed that for 30-μm-spot microarray, each spot contained an average of 1354 UMIs (Fig. 5D), demonstrating the feasibility of the uniform microarray barcoding strategy. These results illustrated the uniformity of the barcoded microarray.

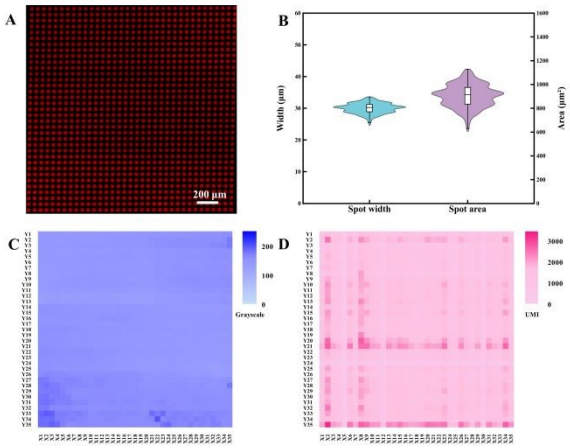

Fig. 5 Characterization of microarray uniformity. (A) Fluorescence image of the microarray; scale bar, 200 μm. (B) Spot width and spot area quantification. (C) Heat map showing the grayscale values of each spot in the microarray fluorescence image. (D) Heat map showing the UMI counts of each spot in the microarray.

Furthermore, the uniform spatially barcoded microarray exhibited scalable potential. From a structural optimization perspective, leveraging the flexibility of microchannel geometries and the fabrication of nanochannels, larger-area microarrays could be developed with higher resolution.[49] From an interface optimization perspective, probe immobilization efficiency could be enhanced through external field-enhanced solid-liquid mass transfer, while three-dimensional nanostructured substrates could be incorporated to increase effective probe binding sites, thereby achieving higher barcode density.[50]

3.4 Uniform spatially barcoded microarray chip for unbiased mRNA detection

To demonstrate the unbiased spatial mRNA capture capability of the uniform spatially barcoded microarray chip, mouse liver mRNA was chosen as a model due to its abundant gene diversity[51]. The mouse liver mRNA was extracted and captured by the spatially barcoded microarray chip, with an RNA integrity number (RIN) of 8.43 (Figure. S8B†). After in situ reverse

transcription, in situ elongation was performed. The second-strand cDNA was amplified, and the amplicons were detected

View Article Online
DOI: 10.1039/D5AN00534E

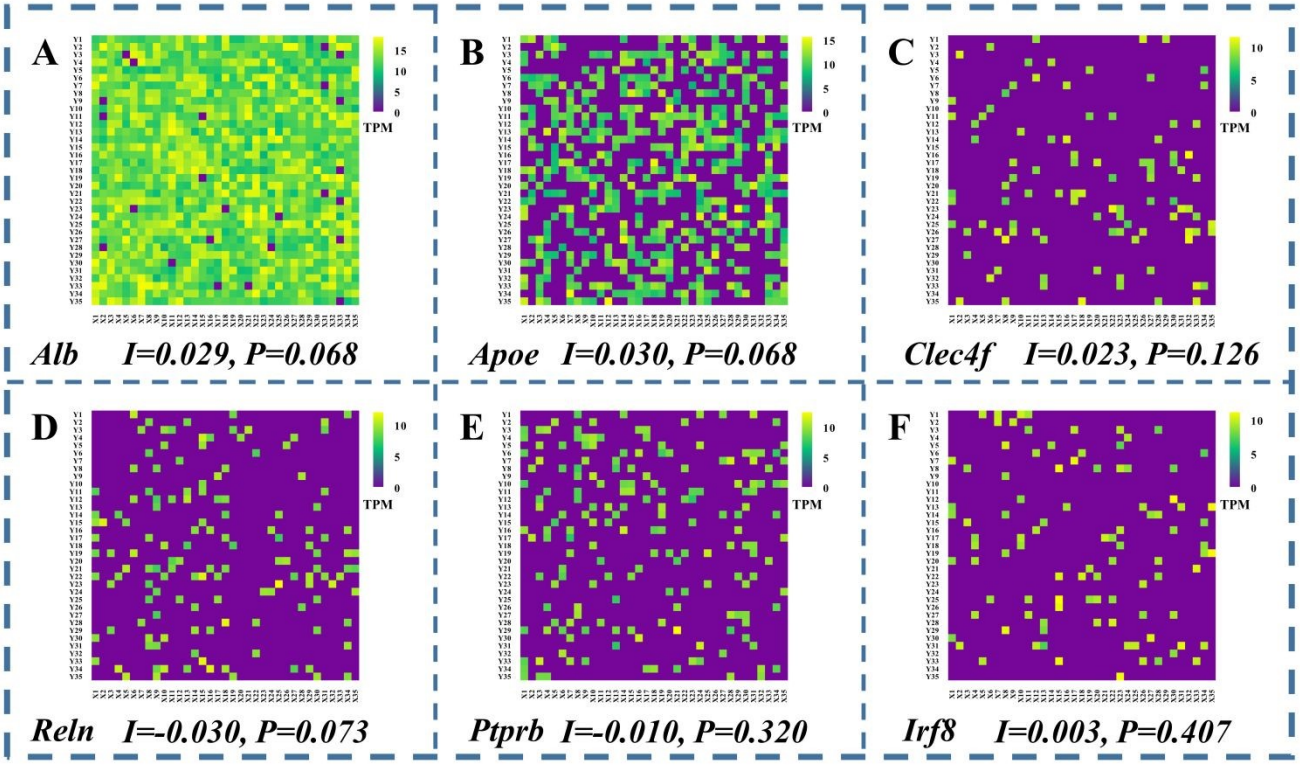

Fig. 6 Spatial unbiased detection of marker genes. The I value represented the Moran's I, while the P value represented the probability that the observed spatial patterns were generated by a random process. The heatmaps displayed the spatial distribution of the marker genes for hepatocytes, macrophages, Kuppfer cells, Hepatic stellate cells, endothelial cells, dendritic cells in the liver, respectively. (A) Alb, (B) Apoe, (C)Clec4f, (D) Reln, (E) Ptprb, (F) Irf8.

using the capillary electrophoresis. The results showed that the mouse liver cDNA was amplified with fragment sizes distributed between 500-1000 bp (Fig. S8C†), demonstrating the mRNA capture capability of the spatially barcoded microarray chip.

Furthermore, we performed NGS of the amplicons to demonstrate the spatially unbiased mRNA capture of the uniform spatially barcoded microarray chip. The results showed that each spot detected an average of 787 genes. However, after denoising, a total of 20173 genes were detected on the chip, which meant that not every spot captured a specific gene. Therefore, we selected marker genes from hepatocytes, macrophages, Kuppfer cells, Hepatic stellate cells, endothelial cells, dendritic cells to verify the spatially unbiased mRNA capture. Alb was a protein coding gene that encoded albumin, primarily synthesized by the liver, and served as a marker gene for hepatocytes.[52] Apoe was a protein coding gene that encoded apolipoprotein E, a key protein involved in lipid metabolism and immune regulation, which served as a marker gene for macrophages.[53] Clec4f was a C-type lectin expressed on Kupffer cells in the liver, which was associated with the regulation of glycolipid presentation and served as a marker gene for Kuppfer cells.[54] Reln encoded Reelin, a glycoprotein that played essential roles in cell migration and served as a marker for hepatic stellate cells.[55] Ptprb encoded protein tyrosine phosphatase receptor type B, which had an important effect in cellular signal transduction and served as a marker gene for endothelial cells.[56] Irf8 was associated with the antigen presentation function of dendritic cells and was selected as a cell marker for this cell type.[53] For each gene, each spot of the uniform spatially barcoded microarray chip should capture it without spatial correlation. Consequently, we transformed the number of genes detected by each spot into a gene expression matrix, visualized the spatial distribution of the transcripts per million (TPM) values for each marker gene as a heatmap, and performed spatial autocorrelation analysis using Moran's I (Fig. 6).[57] The results showed that the weak autocorrelations with absolute values of the global Moran's I below 0.05 were not statistically significant, and revealed that the captured genes were randomly distributed spatially without spatial correlation, demonstrating the spatially unbiased mRNA capture of the barcoded microarray chip.

Conclusions

We have developed the BarSI interface that simultaneously suppresses non-specific adsorption and enables covalent DNA barcode immobilization through the combination of GPTMS and CETES modification. We also grafted mPEG-silane onto PDMS to establish an antifouling layer in the microchannel. We uniformly

View Article Online DOI: 10.1039/D5AN00534E

immobilized DNA barcodes in 40 mm and 60 mm microchannels, with fluorescence intensity CV of 2.3% and 3.2%. Based on the orthogonal barcoding system, we further obtained a spatially barcoded microarray chip, achieving an overall fluorescence intensity CV of 8.47 ± 1.26%. Using the uniform spatially barcoded microarray chip, we successfully captured mouse liver mRNA with the absolute value of Moran's I below 0.05. In conclusion, we provided a low-cost, user-friendly method for fabricating uniform spatially barcoded microarray chips. The chip featured uniformly barcoded spots, offering a new approach for unbiased transcriptome analysis.

Author contributions

Sidi Tian: Conceptualization, Methodology, Validation, Data curation, Writing - original draft. Yingxue Li: Methodology, Validation, Writing – review & editing. Jia Yao: Methodology, Funding acquisition. Changxiang Huan: Software, Data curation. Wei Zhang: Conceptualization, Investigation. Shuli Li: Software, Data curation. Zhiqi Zhang: Funding acquisition, Methodology. Zhen Guo: Funding acquisition, Investigation. Qi Yang: Software. Chao Li: Formal analysis, Validation. Chuanyu Li: Methodology, Supervision, Funding acquisition, Project administration, Writing - review & editing. Jinze Li: Conceptualization, Supervision, Funding acquisition, Project administration, Writing - review & editing. Lianqun Zhou: Conceptualization, Supervision, Funding acquisition, Project administration, Writing - review & editing

Conflicts of interest

There are no conflicts to declare.

Data availability

The data supporting this article have been included in the main text and the ESI.†

Acknowledgements

The acknowledgements come at the end of an article after the conclusions and before the notes and references.
This work was supported by the National Key R&D Program of China (No. 2023YFC2413001), the National Natural Science Foundation of China (No. 52275581, No. 82372142, No. 82327802 and No. 22404171), the Strategic Priority Research Program of Chinese Academy of Sciences (XDC0250000), the Key Research and Development Program of Jiangsu Province (No. BE2022739), the Frontier Technologies R&D Program of Jiangsu Province (No. BF2024030), the Natural Science Foundation of Jiangsu Province (No. BK20240407), the Youth Innovation Promotion Association of CAS (No. Y2022088), the Science and Technology Development Program of Suzhou (No. SYG2024116, No. SJC2021019, No. SSD2023012 and No. SSD2023017), the CAS Key Laboratory of Bio-medical Diagnostics (No. A2023F001), and the Project of Jiangsu Province High-End Medical Devices Technology Innovation Center (No. BM2022012). We would like to express our sincere appreciation to the funding agency for their support.

References

1 A. Baysoy, Z. Bai, R. Satija and R. Fan, Nature Reviews Molecular Cell Biology, 2023, 24, 695–713.
2 J. Ren, S. Luo, H. Shi and X. Wang, Molecular Cell, 2024, 84,3737–3757.
3 S. G. Rodriques, R. R. Stickels, A. Goeva, C. A. Martin, E. Murray, C. R. Vanderburg, J. Welch, L. M. Chen, F. Chen and E. Z. Macosko, Science, 2019, 363, 1463–1467.
4 R. R. Stickels, E. Murray, P. Kumar, J. Li, J. L. Marshall, D. J. Di Bella, P. Arlotta, E. Z. Macosko and F. Chen, Nature biotechnology, 2021, 39, 313–319.
5 A. Chen, S. Liao, M. Cheng, K. Ma, L. Wu, Y. Lai, X. Qiu, J. Yang, J. Xu, S. Hao et al., Cell, 2022, 185, 1777–1792.
6 D. Cipurko, T. Ueda, L. Mei and N. Chevrier, Nature Methods, 2025, 22, 145–155.
7 Y. Liu, M. Yang, Y. Deng, G. Su, A. Enninful, C. C. Guo, T. Tebaldi, D. Zhang, D. Kim, Z. Bai et al., Cell, 2020, 183, 1665–1681.
8 J. Wirth, N. Huber, K. Yin, S. Brood, S. Chang, C. P. Martinez Jimenez and M. Meier, Nature Communications, 2023, 14, 1523.
9 J. Cao, Z. Zheng, D. Sun, X. Chen, R. Cheng, T. Lv, Y. An, J. Zheng, J. Song, L. Wu et al., Nature Biotechnology, 2024, 42, 1735–1746.
10 J. Zhu, K. Pang, B. Hu, R. He, N. Wang, Z. Jiang, P. Ji and F. Zhao, Nature Genetics, 2024, 56, 2259–2270.
11 N. Li, Z. Xu, S. Zheng, H. Dai, L. Wang, Y. Tian, Z. Dong and L. Jiang, Advanced Materials, 2021, 33, 2003559.
12 J. N. Belling, L. K. Heidenreich, J. H. Park, L. M. Kawakami, J. Takahashi, I. M. Frost, Y. Gong, T. D. Young, J. A. Jackman, S. J. Jonas et al., ACS applied materials & interfaces, 2020, 12, 45744–45752.
13 A. Shakeri, S. Khan and T. F. Didar, Lab on a Chip, 2021, 21, 3053–3075.
14 Y. Saad, M. Bouzid, M. Selmi, M. H. Gazzah, A. M. Almansour, A. Y. Boshra, S. M. H. Mansouri and H. Belmabrouk, Sensors and Actuators A: Physical, 2024, 369, 115175.
15 C. Zheng, Z. Hussain, C. Chen, R. J. de Haas, S. Deshpande, Z. Zhang, H. Zuilhof and R. de Vries, Journal of Colloid and Interface Science, 2025.
16 Y. Huang, Z. Liu, X. Qin, J. Liu, Y. Yang and W. Wei, Analyst, 2023, 148, 3295–3305.
17 J. Sun, J. Duan, C. Liu, X. Liu, Y. Zhu, X. Zhai, Y. Zhang, W. Wang, Z. Yang and B. Hou, Chemical Engineering Journal, 2024, 490, 151567.
18 Z. Zhao, M. Pan, C. Qiao, L. Xiang, X. Liu, W. Yang, X.-Z. Chen and H. Zeng, Advanced Materials, 2023, 35, 2208824. 19 W. Choi, S. Park, J.-S. Kwon, E.-Y. Jang, J.-Y. Kim, J. Heo,
19 Y. Hwang, B.-S. Kim, J.-H. Moon, S. Jung et al., ACS nano, 2021, 15, 6811–6828.
20 Y. Li, Q. Xu, W. Zhang, Q. Yang, Z. Guo, C. Li, Z. Zhang, Q. Dong, H. Sun, C. Zhang et al., Sensors and Actuators B: Chemical, 2023, 392, 134112.
21 Q. Kang, C. Wang, K. Liu and T. Kitamori, Lab on a Chip, 2023, 23, 2710–2719.
22 Y. Liang, C. Wang, Z. Liang, L. Zhang and Y. Zhang, Analytical Chemistry, 2022, 94, 6084–6088.
23 P. Giefer, S. Bäther, N. Kaufmes, H. Kieserling, A. Heyse, W. Wagemans, L. Barthel, V. Meyer, E. Schneck, U. Fritsching et al., Journal of Colloid and Interface Science, 2023, 652, 1074–1084.

24 Z. Zhang, Q. Xie, G. Zhang, C. Ma and G. Zhang, ACS Applied Polymer Materials, 2023, 5, 3524–3533.
25 Y. Cao, X. Chen, A. Matarasso, Z. Wang, Y. Song, G. Wu, X. Zhang, H. Sun, X. Wang, M. R. Bruchas et al., ACS applied materials & interfaces, 2023, 15, 9987–9995.
26 Y. Gidi, S. Bayram, C. J. Ablenas, A. S. Blum and G. Cosa, ACS applied materials & interfaces, 2018, 10, 39505–39511.
27 Q. Chen, D. Zhang, J. Gu, H. Zhang, X. Wu, C. Cao, X. Zhang and R. Liu, Acta Biomaterialia, 2021, 126, 45–62.
28 R. Tan, P. Hao, D. Wu, H. Yang, Y. Xia, S. Li, J. Wang, L. Liang, J. Zhou and T. Zhang, ACS Applied Materials & Interfaces, 2023, 15, 41193–41200.
29 J. Qiu, Y. Liang, C. Wang, Y. Yu, Y. Zhang, H. Liu and L. Han, Engineering, 2025, 46, 130–146.
30 J. Xu, H. Chun, L. Wang, H. Mei, S. Chen and X. Huang, Chemical Engineering Journal, 2024, 499, 155937.
31 X. Lu, S. Lee, J. Kim, N. Abbas, M. A. Badshah and S.-m. Kim, Biosensors and Bioelectronics, 2021, 175, 112881.
32 C. Liu, L. Yang, Q. Niu, G. Yu and G. Li, New Journal of Chemistry, 2022, 46, 4300–4306.
33 M. McKenna, F. Soberon, A. J. Ricco, S. Daniels and S. M. Kelleher, Sensors and Actuators B: Chemical, 2016, 236, 286–293.
34 H. Yousefi, H.-M. Su, M. Ali, C. D. Filipe and T. F. Didar, Advanced Materials Interfaces, 2018, 5, 1800659.
35 L. Gogianu, M. C. Popescu, B. S. Vasile, I. Mihalache, E. M. Anghel, C. M. Damian, A. Salceanu, A. Boldeiu, E. Constantin, A. Radoi et al., Applied Surface Science, 2023, 636, 157878.
36 Q. Wu, M. Niu, D. Ren, L. Yi, K. Ge and Y. Gu, Talanta, 2024, 271, 125623.
37 Y. Zhang, L. Wang, N. Ma, Y. Wan, X. Zhu and W. Qian, Langmuir, 2023, 39, 11406–11413.
38 Z. Tu, M. Liu, C. Xu, Y. Wei, T. Lu, Y. Xiao, H. Li, S. Zhang, X. Xie, J. Li et al., Advanced Science, 2024, 11, 2307800.
39 X. Xie, X. Chen, P. A. Levkin and W. Feng, Advanced Materials, 2022, 34, 2203619.
40 J. Li, L. Li, X. Du, W. Feng, A. Welle, O. Trapp, M. Grunze, M. Hirtz and P. A. Levkin, Nano letters, 2015, 15, 675–681.
41 P. Jiménez-Meneses, M.-J. Bañuls, R. Puchades and Á. Maquieira, Analytical chemistry, 2018, 90, 11224–11231.
42 Z. Ma, X. Ye, y. Shang, D. min et al., Optics and Precision Engineering, 2013, 21, 1988–1994.
43 A. Das, S. Santhosh, M. Giridhar, J. Behr, T. Michel, E. Schaudy, G. Ibáñez-Redín, J. Lietard and M. M. Somoza, Analytical Chemistry, 2023, 95, 15384–15393.
44 Z. Zhang, X. Feng, Q. Luo and B.-F. Liu, Electrophoresis, 2009, 30, 3174–3180.
45 M.-C. B. Salon and M. N. Belgacem, Colloids and Surfaces A: Physicochemical and Engineering Aspects, 2010, 366, 147–154.
46 H. Liu, M. Fukuyama, Y. Ogura, M. Kasuya, S. Onose, A. Imai, K. Shigemura, M. Tokeshi and A. Hibara, Analyst, 2024, 149, 5139–5144.
47 D. Zhang, W. Dai, H. Hu, W. Chen, Y. Liu, Z. Guan, S. Zhang and H. Xu, Nanoscale, 2021, 13, 4269–4277.
48 Q. He, L. Zhang, P. Han, M. Fu and G. Zhu, Process Safety and Environmental Protection, 2024, 184, 391–399.
49 W. Sun, Y. Xiao, P. Yan, F. Sun, X. Zhang, C. Sheng, Q. Wang and Y. Yu, Nano Research, 2025, 18, 94907098.
50 Y. M. Shlyapnikov, E. A. Malakhova and E. A. Shlyapnikova, Analytical Chemistry, 2020, 93, 1126–1134.
51 J. Xu, P. Guo, S. Hao, S. Shangguan, Q. Shi, G. Volpe, K. Huang, J. Zuo, J. An, Y. Yuan et al., Nature genetics, 2024, 56, 953–969.
52 K. B. Halpern, R. Shenhav, O. Matcovitch-Natan, B. Tóth, D. Lemze, M. Golan, E. E. Massasa, S. Baydatch, S. Landen, A. E. Moor et al., Nature, 2017, 542, 352–356.
53 J. Wang, W. Hu, Z. Shen, T. Liu, W. Dai, B. Shen, X. Li, J. Wu, L. Lu, S. Li et al., Molecular Therapy Nucleic Acids, 2021, 26, 1364–1373.
54 C.-Y. Yang, J.-B. Chen, T.-F. Tsai, Y.-C. Tsai, C.-Y. Tsai, P.-H. Liang, T.-L. Hsu, C.-Y. Wu, M. G. Netea, C.-H. Wong et al., PloS one, 2013, 8, e65070.
55 F. Hildebrandt, A. Andersson, S. Saarenpää, L. Larsson, N. Van Hul, S. Kanatani, J. Masek, E. Ellis, A. Barragan, A. Mollbrink et al., Nature communications, 2021, 12, 7046.
56 M. L. Richter, I. Deligiannis, K. Yin, A. Danese, E. Lleshi, P. Coupland, C. A. Vallejos, K. Matchett, N. Henderson, M. Colome-Tatche et al., Nature communications, 2021, 12, 4264.
57 E. Zormpas, R. Queen, A. Comber and S. J. Cockell, Cell, 2023, 186, 5677–5689.

View Article Online
DOI: 10.1039/D5AN00534E

Data Availability Statement

The data supporting this article have been included in the main text and the ESI.